RESEARCH ARTICLE

ADVANCED OPTICAL MATERIALS
www.advopticalmat.de

Light-Induced Colossal Magnetoresistance and Ultrasensitive Hall Resistance of Intrinsic Silicon

Zhigang Li, Tianle Wang, Jalil Varela-Manjarres, Kapildeb Dolui, Yanping Liu, Minghu Fang, Shangshen Feng,* Branislav K. Nikolić,* and Bingqing Wei**

Due to their unique energy level structure and high kinetic energy, photoexcited hot carriers exhibit excellent performance from thermally excited carriers in semiconductors. Here, the electrical transport properties of photoexcited hot carriers in intrinsic monocrystalline silicon at 10 Kelvin, where traditional thermally excited carriers can be neglected are reported. Compared to thermally excited carriers, hot carriers exhibit several notable differences: an increase in carrier mobility of ≈2–3 orders of magnitude, up to ≈10^6 cm^2 Vs^{-1}; an increase in magnetoresistance of ≈5 orders of magnitude, up to ≈6.4×10^4 % at 1 Tesla, which is more prominent than almost all topological materials under the same conditions, and a novel hot-carrier-dependent Hall effect with ultrahigh linear Hall field sensitivity (≈ 3.2×10^7 Ω T^{-1}) is observed. The large measured magnetoresistance is replicated by Floquet–Keldysh quantum transport simulations of the light-irradiated two-terminal gapped device, provided that it includes spin-orbit coupling (SOC). While SOC effects are minor in intrinsic Si, it is interpreted as additional ones arising due to inversion symmetry breaking in the effective heterostructure photoexcited-Si/plain-Si. These findings exemplify a new paradigm of light-induced phenomena in a mundane solid-state material, opening new avenues for light-driven, low-power consumed, and ultrahigh field sensitivity hot carrier devices.

1. Introduction

The photoelectric effect is a classical quantum phenomenon that enables electrons in a semiconductor to gain higher velocity and momentum by absorbing photon energy and leaving their original positions to form hot electron-hole charge pairs,[1–4] whose energy can be more significant than thermal excitations. In many fields, from photovoltaics[5–7] to photodetection,[8–10] hot carriers, only a small fraction of the material's charge carriers, play a critical role in material performance due to their unique wavelength-dependent energy level structure[1,4] and high kinetic energy.

The mixed states of photoexcited-hot/thermally-excited carriers have been well studied;[11,12] however, the states of the hot carrier systems, such as hot carrier effective mass and velocity, hot electron-hole interaction, etc., are still under scrutiny. Monocrystalline Si, widely used as an intrinsic semiconductor in functional devices and computer chips,[13–15] allows for exploring the transport properties of photoexcited hot carriers at lower temperatures (10 K) under light illumination because the ordinary electron-hole pairs excited thermally at an ambient temperature can be neglected.

This study investigates the transport properties and the relationship between the magnetic field and resistance of photoexcited hot carriers in intrinsic monocrystalline silicon at 10 K. The nonequilibrium hot carriers exhibit several surprising effects: high charge carrier mobility (≈ 10^6 cm^2 Vs^{-1}), an ultrahigh magnetic field sensitivity in both vertical (Hall field sensitivity, ≈ 3.2×10^7 Ω T^{-1}) and

Z. Li, T. Wang, Y. Liu
School of Materials Science and Engineering
Taizhou University
Taizhou 318000, China
E-mail: lizhigang@issp.ac.cn

J. Varela-Manjarres, B. K. Nikolić
Department of Physics & Astronomy
University of Delaware
Newark, DE 19716, USA
E-mail: bnikolic@udel.edu

The ORCID identification number(s) for the author(s) of this article can be found under https://doi.org/10.1002/adom.202403577

[+]Present address: Department of Physics, Indian Insititute of Technology Tirupati, Tirupati, Andhra Pradesh 517619, India

DOI: 10.1002/adom.202403577

K. Dolui[+]
Department of Materials Science and Metallurgy
University of Cambridge
Cambridge CB30FS, UK

M. Fang
Department of Physics
Zhejiang University
Hangzhou 310027, China

S. Feng
School of Science
Zhejiang Agricultural and Forestry University
Hangzhou 311300, China
E-mail: fengss@zafu.edu.cn

B. Wei
Department of Mechanical Engineering
University of Delaware
Newark, DE 19716, USA
E-mail: weib@udel.edu

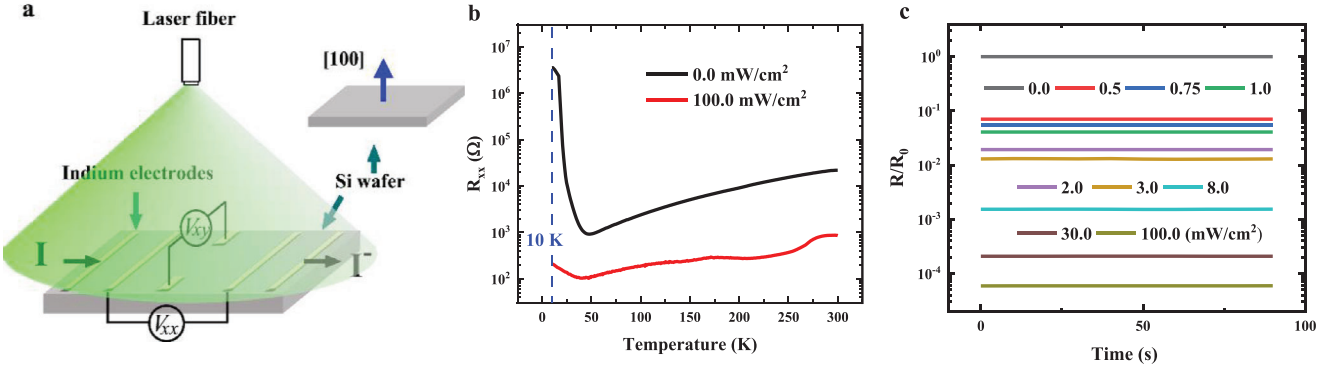

Figure 1. Si sample setup, structure, and light-dependent resistance. a) Schematics of the experimental setup for transport property measurement. The Si wafer sample is ≈10 × 2.5 × 0.5 (mm) with six In electrodes. b) Temperature-dependent resistance with/without light illumination along the wafer surface. c) Resistance relaxation under different light power densities at 10 K. R_0 denotes R_{xx} resistance without light illumination.

horizontal (colossal magnetoresistance under 1 Tesla is of ≈6.4 × 10^4 %) resistance and a significantly enhanced spin-orbit coupling (SOC) in monocrystalline photoexcited Si (which is otherwise a material with weak SOC in equilibrium, i.e., when light is absent). Our findings exemplify a new paradigm of light-induced hot carrier systems in Group IV materials, opening new avenues for light-controlled, low-power consumed, and ultrahigh field sensitivity hot carrier devices.

2. Results and Discussion

2.1. Light-Induced Colossal Magnetoresistance and Hall Resistance at 10 K

A monocrystalline Si wafer with orientation [100], as shown in **Figure** 1a, was chosen to characterize the transport behavior, including magnetoresistance (MR) and Hall resistance (HR) at low temperatures under a laser illumination with a wavelength of 520 nm. A monochromatic laser provides an ideal condition to investigate the hot carriers by ensuring they have the same energy ΔE (ΔE = $\hbar\omega - E_g$, where $\hbar\varpi$ represents phonon energy, and E_g signifies the bandgap of Si ≈1.12 eV). For a 520 nm laser, the ΔE is ≈1.26 eV.

The temperature-dependent resistance of the Si wafer with/out light illumination (0 and 100 mW cm^{-2}) is shown in Figure 1b. At a low temperature of 10 K, the resistances with/out the light illumination vary greatly: from ≈ 3.5 × 10^6 Ω without the light irradiation to209 Ω with a light power density of 100 mW cm^{-2}, indicating an extreme light sensitivity of resistance of intrinsic Si at a low temperature. It is important to note that light-induced hot charge carriers diffuse isotropically and rapidly move from the surface of the Si wafer into the bulk. High resistance is quickly restored without light excitation, indicating the extremely short lifetime of hot carriers. The inversely proportional light power-dependent resistance demonstrated in the resistance relaxation curves in Figure 1c shows that the resistance variation is instantaneous, and the resistance remains stable under the same light power density (≤100 mW cm^{-2}). Higher light power density, i.e., 200 mW cm^{-2}, might result in an instability of the resistance due to the heat effect (Figure S1, Supporting Information). This paper only discusses data with less than 100 mW cm^{-2} light intensity to avoid the thermal light-induced impact.

Light power-dependent MR of the wafer at 10 K is shown in **Figure** 2a, where MR is defined as MR = (R_B-R_0) /R_0, and R_B is the resistance in the applied magnetic field, B. With the increase of light power density from 0 to 15 mW cm^{-2} 1/7 of midday sunlight intensity) in a magnetic field of B = 1 T, MR can be dramatically enhanced from 0.3% to 63,766%,2.1 × 10^5 fold increase, which is significantly larger than most of the topological materials (TMs)[16] at 1 T, such as WTe_2 (≈7 × 10^3%),[17] NbP (≈1.8 × 10^4%),[18] and α-Ga (≈3.7 × 10^4%).[19]

Unlike the non-saturated MR of TMs, all the light-induced MR in Si can reach a saturated state under different magnetic fields B_{sat} (Figure S2, Supporting Information). Interestingly, the saturated field (SF) increases linearly proportional to the square root of the light power density (Figure 2b). Moreover, when MR reaches saturation at value MR_{sat}, the longitudinal resistances R_{xx} under different light power densities hold similar values, i.e., 3.4 ± 0.4 × 10^6 Ω (Figure S1, Supporting Information, and some raw data are provided in Figure S3, Supporting Information).

Light power-dependent HR at 10 K is shown in Figure 2c, which mainly focuses on the unsaturated part, and the original HR data are provided in Figure S2 (Supporting Information). HR is very small without light illumination due to the normal HE of ordinary charge carriers. Under light illumination, HR is similar to an anomalous Hall effect (AHE) and increases drastically as a function of the magnetic field, in particular under a low light power density of 0.01 mW cm^{-2}, but with a substantial HR variation-the HR is approximately linear to the external magnetic field within ± 0.03 T and saturates at ≈ 1.0 × 10^6 Ω beyond 0.03 T. The slope of the HR field response, i.e., the field sensitivity of the Hall effect (S_H), reaches as high as 3.2 × 10^7Ω T^{-1}, the most significant linear field sensitivity so far, is ≈ 3 orders of magnitude higher than that of AHE in multilayers MgO/CoFeB/Hf/Ta/MgO (≈2.8 × 10^4 Ω T^{-1}, the largest S_H in AHE materials).[20] The ultrahigh S_H, as well as the linear relationship with the magnetic field, make it highly promising to develop ultrasensitive magnetic sensors and detect weak magnetic fields. Akin to MR, the SF of HR is also proportional to the square root of the light power density, as shown in Figure 2d. However,

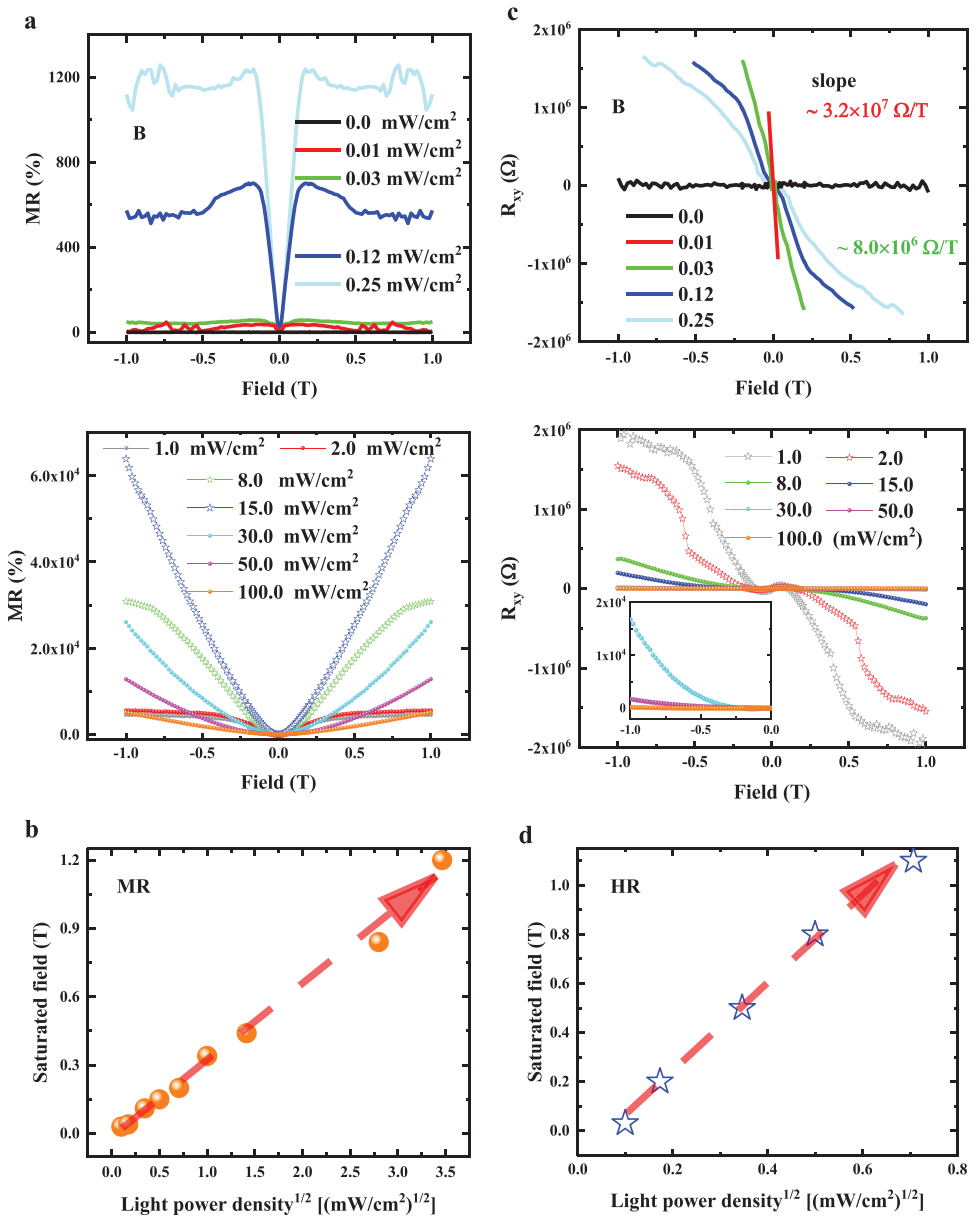

Figure 2. Light power-dependent MR and HR at 10 K of an intrinsic Si wafer. a) MR with a magnetic field perpendicular to the sample. b) Light-induced SF of MR. c) HR (unsaturated) with a magnetic field perpendicular to the sample, the inset is the magnification at the power densities of 30.0, 50.0, and 100.0 mW cm^{-2}. d) Light-induced SF of HR. The red arrows show that the SFs, both MR and HR, are approximately proportional to the square root of the light power density.

the SF of HR differs from that of MR under the same light power density.

The light-induced MR and HR properties were also investigated in control Si samples: a monocrystalline Si with an orientation [111] and a polycrystalline Si with the same size as the orientation [100] Si (Figure S4, Supporting Information). For [111] Si, significant MR and HR are also observed. The SF of MR is linearly proportional to the square root of the light power density. For the polycrystalline Si, however, MR is less than one-eighth of the monocrystalline Si [100] under the same light power density, indicating that such light-induced properties are sensitive to the degree of Si crystallinity.

2.2. The Effective Film and Hot Carrier Density and Mobility

Under laser irradiation at 10 K, R_{zz} is 0.2 MΩ, while R_{xx} is ≈200 Ω (**Figure 3a**), R_{xx} is only 1/1000 that of R_{zz}, demonstrating that the hot carriers are mainly constrained near the surface (within the light penetration depth) of the Si wafer and their diffusion into the crystal's bulk can be neglected. Figure 3b confirms that ≈95% of the light is mainly trapped within 2 microns of the Si wafer surface, indicating that most photoexcited hot carriers are generated within the top 2 microns of the Si wafer surface.

It is well understood that in the mixed states of photoexcited-hot/thermally-excited carriers, hot carriers can rapidly diffuse

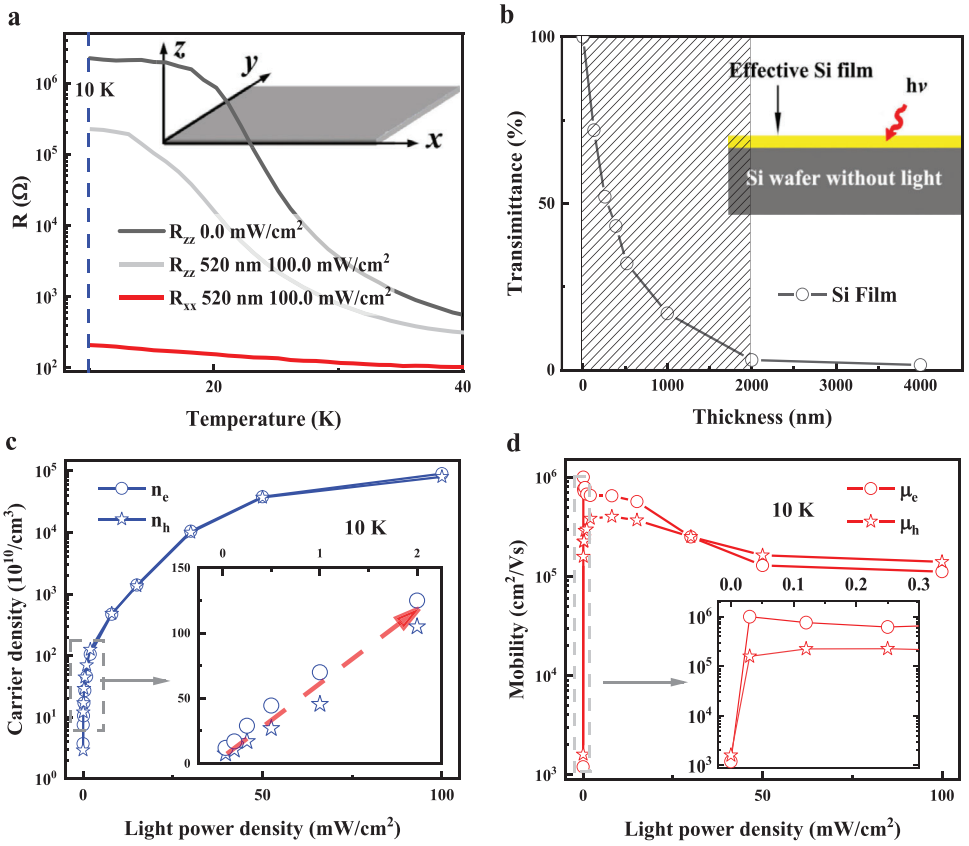

Figure 3. Light absorption of Si and charge carrier density and mobility. a) The resistance of Si along different directions at low temperatures. The inset is a directional diagram. b) Light transmission spectra with varying thicknesses of Si films. The shaded area demonstrates that most light, i.e., ≈95%, is trapped within the 2-micron thickness range. The inset is a schematic diagram of the EF of Si. c) The light-power-density dependence of hot carrier density, where the inset is the magnification of carrier density from 0 to 2.0 mW cm^{-2} light power density. d) The light power-density-dependent of hot carrier mobility, where the inset is the magnification of carrier mobility from 0 to 0.3 mW cm^{-2} light power density. Both carrier density and mobility were calculated based on the Si effective film. Here, n_e (n_h) and μ_e (μ_h) denote the carrier densities and mobilities of electrons (holes), respectively. The fitting curves are shown in Figure S5 (Supporting Information).

into the bulk of the crystal to recombine with the uniformly presented thermally excited carriers. However, hot carriers typically have short lifespans and can not survive without light. Continuous light irradiation within the light penetration depth of microns produces new hot carriers, which will survive, dominate the transport behavior along the R_{xx} direction, and decrease the drastic resistance. Therefore, a simple and justifiable model with an effective film (EF) thickness of 2 microns (≈95% light absorption) is employed to estimate charge carrier density and mobility: the most photoelectric effect is assumed to be the same everywhere within the EF under light illumination. In contrast, the photoelectric effect underneath the EF can be neglected.

Figure 3c,d displays the light power-density-dependence of carriers' density and mobility at 10 K using the two-carrier model.[21,22] Both electrons and holes increase synchronously with the increase in light power density. The inset in Figure 3c reveals that the hot carrier densities are proportional to the light power density. More striking, the mobility of electrons increases by ≈3 orders of magnitude from ≈ 1200 cm^2 Vs^{-1} (without light illumination) to ≈1 × 10^6 cm^2 Vs^{-1} under the light power density of 0.03 mW cm^{-2}, see the inset in Figure 3d. The holes' mobility increases by 2–3 orders of magnitude, indicating that hot electron-hole pairs under light illumination dominate the charge carriers. Similarly, the mobility of hot carriers in the control Si [111] sample also increases by 2–3 orders of magnitude of the ordinary charge carriers (Figure S6, Supporting Information). Here, the carrier density is approximately proportional to the light power density. It has been shown that high mobility can significantly enhance the performance of electronic devices. For instance, the power conversion efficiency of Si solar cells has been observed to double at extremely low temperatures due to high mobility.[23]

It should be noted that the hot carriers' density will gradually decrease from the Si surface to the inside, but the carriers' mobility does not show a noticeable change. This conclusion is drawn by applying different effective film thicknesses, as shown in Figure S7 (Supporting Information), where the hot electrons' density and mobility have been calculated based on the EF thicknesses of 1 (≈82% light absorption), 2 (≈95% light absorption), 4 (≈99% light absorption), and 10 μm (≈99.9% light absorption).

Such ultrahigh mobility should be attributed to hot carriers' high velocity and momentum (here, the kinetic energy of hot electrons is ≈1.2 eV, far above that of thermally excited electrons), which enhance the SOC of intrinsic Si.

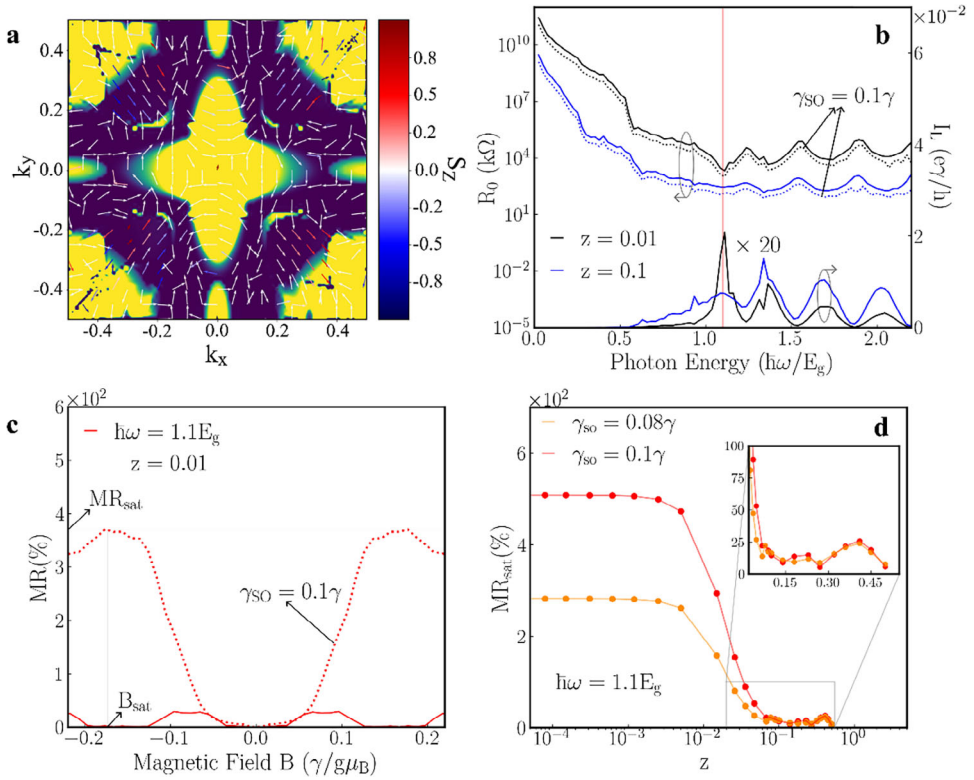

Figure 4. DFT-GF or Floquet-Keldysh-GF simulations of semi-infinite Si in equilibrium and light-irradiated two-terminal device out of equilibrium, respectively. a) Spectral function (yellow) and spin-momentum-locked spin texture (arrows) at $E = 1.9$ eV (equivalent to an absorbed photon energy of 520 nm) computed[29,30] on the surface of semi-infinite Si (100) and within the first Brillouin zone of momenta. The out-of-plane *z*-component of the vectors of the electronic spin expectation value is indicated by blue or red color (using the color bar on the right of panel d). b) Resistance (left ordinate) and photocurrent versus frequency of applied laser light for the different magnitudes of its electric field (black lines for $z = 0.01$ and blue lines $z = 0.1$). Dotted resistance lines include the Rashba SOC ($\gamma_{so} = 0.1\gamma$ in Equation 4) within the active region of the device irradiated by light, while the vertical red line marks frequency $\hbar\omega = 1.1E_g$, at which quantities in (c)–(d) are plotted. c) MR as a function of applied perpendicular magnetic field in the absence (solid line) and presence (dotted line) of the Rashba SOC. d Saturated value of magnetoresistance MR_{sat}, also marked in panel b and achieved at the magnetic field B_{sat}, as a function of the light electric field for two different values of the Rashba SOC. Here, z is the dimensionless magnitude of the light electric field.

2.3. Floquet–Keldysh Quantum Transfer Simulations of Hot Carriers Subjected to SOC

Due to the small atomic number and inversion symmetric in the bulk crystalline lattice, SOC in intrinsic Si is weak,[14] including for hot charge carriers.[24] Nevertheless, the measured colossal MR in Figure 2 suggests that hot charge carriers are subjected to significant SOC. Indeed, if SOC is included in the Floquet-Keldysh quantum transfer simulations (with details introduced below) of the light-irradiated gapped two-terminal device, we replicate a significant enhancement of MR in **Figure** 4c. We attribute the origin[25,26] of SOC to inversion symmetry breaking in the effective heterostructure photoexcited Si/plain-Si. That is, photoexcited hot charge carriers are present within less than two microns (for the laser light of 520 nm wavelength) thick region of intrinsic Si, which represents the photoexcited-Si layer whose light-dressed Floquet bands[27,28] are quite different from the remaining plain-Si layer with no light reaching it.

We confirm the idea that hot charge carriers can experience significant SOC in Si with such effective inversion symmetry breaking by using first-principles Hamilton from density functional theory (DFT) of semi-infinite Si, where inversion symmetry breaking is introduced by Si/vacuum interface, with the retarded Green's function (GF) expression[29,30] for spectral function (Figure S8a, Supporting Information) and spin textures (Figure 4a; Figure S7b, Supporting Information). These quantities are computed on the surface of semi-infinite Si or 15 Å under it (Figure S8b, Supporting Information) at energies in the Si conduction band to which valence electrons will be promoted by absorbing photons energy of 520 nm. The nonzero spin texture in Figure 4a, where arrows denote the expectation value of the spin operator in eigenstates of the conduction band and signify spin-momentum locking as the hallmark of SOC, confirms that hot charge carriers will be subjected to significant SOC.

Despite recent experimental and applicational interest in photocurrent-dependent phenomena in light-illuminated semiconductors and 2D materials,[31] theoretical explanations of such phenomena have been largely qualitative or based on phenomenological equations.[31] A proper microscopic understanding of photocurrent, which would start from a Hamiltonian of a two-terminal device irradiated by light, can be achieved via the Floquet formalism for periodically driven quantum systems,[32]

combined with quantum transport techniques as offered by Keldysh GF.[33] However, studies of Floquet engineering of different materials have been largely focused on discovering exotic phases, such as Floquet topological insulators,[34] in quantum materials driven by light. An exception is Ref. [35], where periodically driven semiconductor nanowires were examined theoretically to find electron-hole metals and Floquet insulators depending on the strength of the driving light field, but without computing photocurrent. Thus, to explain experimental data, the resistance and magnetoresistance of photocurrent were studied by applying the Floquet-Keldysh GF[36,37]to the two-terminal device (Figure S9, Supporting Information) where a finite length 1D Rice-Mele tight-binding (TB) chain[38,39] is the active (middle) region, generating energy gap for the whole device akin to the gap of Si (inset in Figure S9, Supporting Information) and irradiated by continuous laser light of frequency ω. This active region, whose Hamiltonian Equation (4) can include Rashbar SOC,[25,26] motivated by the discussion above and Figure 4a, or the magnetic field needed to study MR in Figure 2, is attached to two nonirradiated semi-infinite metallic electrodes (modeled as 1D TB chains[38] as well) terminating in macroscopic reservoirs with the chemical potential difference $\mu_s - \mu_d = eV_{sd}$ between the source and the drain reservoirs. Using such a setup, ensuring a continuous energy spectrum brought by the semi-infinite leads is crucial to evade unphysical effects like heating[34] of the active region and ever-increasing photocurrent.[40]

Figure 4b demonstrates a significant increase in photocurrent when the frequency of light is larger than the gap, leading to a drop in device resistance by many orders of magnitude in full accord with experimental data (Figure 1b). However, nonzero photocurrent is also observed when the frequency of the light reaches half of the gap, on the proviso that its electric field is sufficiently strong as measured by the z parameter in Equation (5). This indicates higher-order processes, such as two-photon absorption,[38] where an electron from the valence band absorbs two photons simultaneously to transition to the conduction band so that photocurrent is the square of light intensity (or $\approx z^4$). While including the Rashba SOC within the Rice-Mele chain does not affect the resistance in Figure 4b, it dramatically enhances the MR of the device in Figure 4c, especially in the high magnetic field. It should be noted that the light-tunable SOC plays a crucial role in further improving the MR in addition to the n-p carriers' compensation observed in the nonsaturated MR of TMs.[17–19] It explains that the MR of hot carriers is significantly larger than most TMs under the same conditions. Although the Rashba SOC as the origin of MR in metals has been observed recently,[41] the effect therein was tiny (≪1%). To further explain factors affecting MR, the variation of its maximum (or saturated) value MR_{sat} (also marked in Figure 4c) is plotted in Figure 4d.

2.4. Understanding the Transport Characteristics of Hot Carriers

Despite their short lifetimes, hot carriers can reach a specific density to maintain a stable dynamic equilibrium under a particular light power density. Assuming the photoexcited hot carriers are uniformly distributed within the EF, the average distance ($\bar{l}$) between hot holes depends on the carrier density and can be calculated (Table S1, Supporting Information) at different light power densities. Si^+ ions are employed in place of hot holes to schematically illustrate the distribution of hot holes due to their equivalence (**Figure 5a**). Due to the escape of an excited electron from a Si atom with sp^3 hybridization, the Si^+ structure diverges from the sp^3 hybridization and tends toward sp^2 hybridization, resembling the low-buckled structure of silicene.[42,43] When $\bar{l}$ is larger than the EF thickness, the distribution of Si^+ could be considered a quasi-monatomic layer, which plays a crucial role in the transport properties of hot carriers.

When a magnetic field is applied, the Lorentz force drives a hot electron to move in a circle (Figure 5b) with a cyclotron radius (r) $r \times qB = m_h^* v_h$. Here, m_h^* and v_h are the effective mass and velocity of hot electrons, respectively. When $\bar{l} \approx 2r$, it corresponds to a critical field, i.e., the SF, beyond which, i.e., $\bar{l} > 2r$, hot electrons will be localized and cannot recombine with neighbor holes (Figure 5b). Then, the dominant charge carriers will return to thermally excited carriers. Thus, both R_{xx} and R_{xy} will revert to a high resistance state like the one without light, as the observed saturated $R_{xx}[(R_{xx})_S]$ and R_{xy} $[(R_{xy})_S]$ (Figure S2, Supporting Information). The $(R_{xx})_S$ and $(R_{xy})_S$ are $\sim$ 3.4 ± 0.4 ($\times 10^6$ Ω) and 1.3 ± 0.3 ($\times 10^6$ Ω) respectively, which equal the resistances in longitudinal (3.5×10^6 Ω) and transversal (1.4×10^6Ω) electrodes (Figure 1a) without light illumination, respectively. Therefore, it explains the observations that the SFs, both MR and HR, are approximately proportional to the square root of the light power density, which is proportional to the carrier density (Figures 2b,d, and 3c) in the 2D EF layer.

If $\bar{l} < 2r$, the hot electrons will recombine with neighbor hot holes, and significantly high carrier mobility can be observed (Figure 3c), resulting in relatively low resistance. An ultrahigh S_H, expressed as $(R_{xy})_S$/SF, can be observed under a lower light power density due to its relatively small SF (Figure 2d). In addition, MR could also arise from the balanced carriers' resonance' condition.[18,44,45]

3. Conclusion

In summary, we characterized the electric transport properties of photoexcited hot carriers in intrinsic monocrystalline Si at 10 K. These unusual hot carriers exhibit ultrahigh magnetic field sensitivity in both vertical (HR) and horizontal (MR) resistance. Our microscopic Floquet-Keldysh theory of photo-assisted quantum transport explains resistance decrease over many orders of magnitudes once the light is applied, while reproduced colossal MR increase reveals that hot charge carriers exhibit a significantly enhanced SOC in the conduction band of Si, which, furthermore, is tuned by the applied light. Our simple method allows one to study the rich physics of hot carriers in far-from-equilibrium materials while paving the way for developing light-control, low-power-consumption, and ultra-sensitive quantum devices.

4. Experimental Section

Materials: Monocrystalline Si wafers were purchased from Zhejiang Jingli Corporation. The silicon wafer samples with the size of 2.5 mm × 10.0 mm × 0.5 mm were ultrasonically cleaned in acetone and subsequently in ethanol for 10 min, then soaked in 2% hydrofluoric acid for 0.5 h to remove the surface silica at 4 °C to prevent the destruction of the

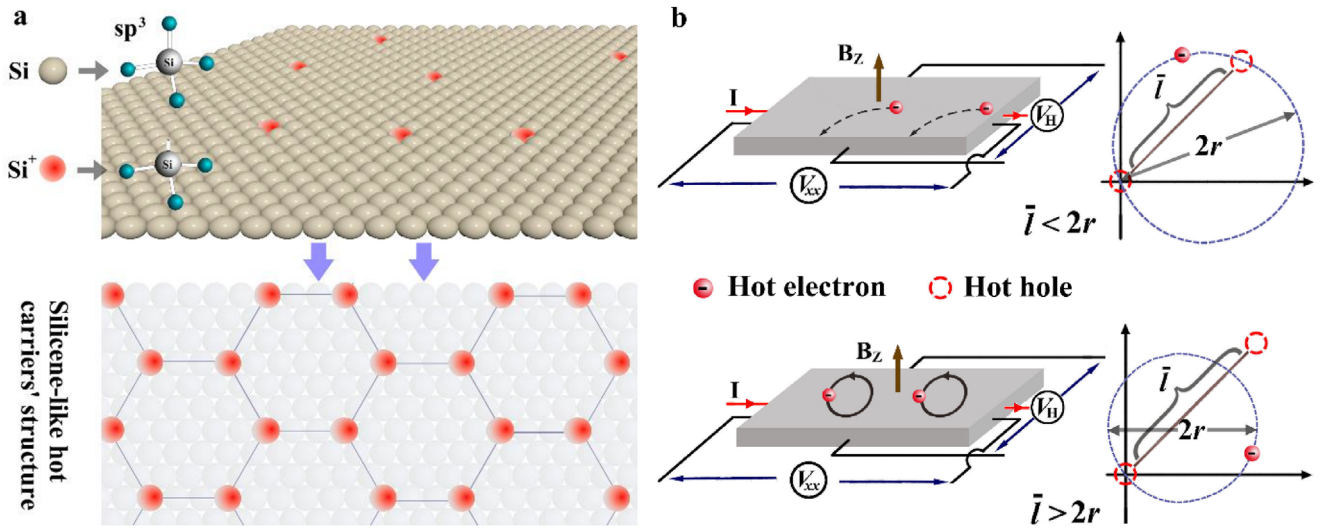

Figure 5. Light-induced hot charge carriers in Si. a) Hot carriers are distributed in the EF of Si, and an equivalent ideal hot carrier silicene-like structure is formed where the gray balls denote Si atoms, and the red balls represent Si^+. b) MR and HE hot carriers in an applied magnetic field, where $\bar{l}$ is the average distance between the holes, $2r$ is the circle diameter under Lorentz force, and V_H is the Hall voltage.

monocrystalline feature. The 520 nm diode laser (LR-MFJ-520/600 mW) with a power range from 0 to 600 mW was purchased from Changchun Laser Technology Co.

Morphological and Property Characterization: The crystal characterization was performed on an X'Pert Pro XRD system with X-ray Mirror PFX at an operation voltage of 40 kV and a current of 40 mA, in which Cu Kα radiation ($\lambda = 0.154059$ nm) was used and scanned in a 2θ range from 20° to 90°. The transport properties of samples were measured with a physical property measurement system (PPMS) equipped with an optical fiber (working temperature range from 350 to 10 K) that can pass through a wavelength range from 300 to 1400 nm. A power tunable diode laser with a wavelength of 520 nm was perpendicularly applied to the sample surface to induce transport properties of the Si samples with a current of 1 μA. The optical absorption/transmission spectra were recorded at room temperature on a Hitachi U-4100 UV–vis–NIR spectrophotometer within 200–2400 nm. It should be noted that the measurements of these samples demonstrated satisfactory repeatability. Analysis of ≈16 samples revealed highly consistent results.

Carriers' Density and Mobility are Calculated Using the Two-Carrier Model: In this model, the conductivity tensor in its complex representation is given as[17]

$$\sigma_{xy} = \frac{en_e\mu_e}{1 + i\mu_e\mu_0 H} + \frac{en_h\mu_h}{1 + i\mu_h\mu_0 H} \tag{1}$$

where n_e (n_h) and μ_e (μ_h) denote the carrier densities and mobilities of electrons (holes), respectively. To appropriately evaluate the carrier densities and mobilities, the Hall conductivity $\sigma_{xy} = -\rho_{xy}/(\rho_{xx}^2 + \rho_{xy}^2)$ and the longitudinal conductivity $\sigma_{xx} = \frac{\rho_{xx}}{\rho_{xx}^2+\rho_{xy}^2}$ were calculated using the original experimental $\rho_{xy}(H)$ and $\rho_{xx}(H)$ data based on the Si monocrystalline cells. Then, both σ_{xy} and σ_{xx} were given by[21,22,46]

$$\sigma_{xy} = \frac{e\,(\mu_0 H)\,n_h\mu_h^2}{1 + \mu_h^2(\mu_0 H)^2} - \frac{e\,(\mu_0 H)\,n_e\mu_e^2}{1 + \mu_e^2(\mu_0 H)^2} \tag{2}$$

$$\sigma_{xx} = \frac{en_h\mu_h}{1 + \mu_h^2(\mu_0 H)^2} + \frac{en_e\mu_e}{1 + \mu_e^2(\mu_0 H)^2} \tag{3}$$

where n_e (n_h) and μ_e (μ_h) denote the carrier densities and mobilities of electrons (holes), respectively. $\rho_{xy}(H)$ and $\rho_{xx}(H)$ can be obtained by $\rho_{xy(xx)} = R_{xy(xx)} \times S/l_e$. Here, S is the cross-sectional area of the effective film, and the l_e is the distance between the measuring electrodes. Only unsaturated parts of the original R_{xx} and R_{xy} were used in the two-carrier model. The experimental data agree well with the two-carrier model over a wide conductivity range, confirming a significant change in carrier density and mobility of both electrons and holes.

First-Principles GF Calculation of Spectral Function and Spin-Momentum-Locked Spin Textures: The spectral function and spin textures on the surface of semi-infinite Si[100] were computed by using DFT combined with the retarded GF calculations, $G(E;\ k_x, k_y, z)$, in mixed real and k-space representation, as elaborated in Refs. [29,30], and implemented in Quantum ATK package.[47] The Kohn–Sham Hamiltonian is obtained from non-collinear DFT calculations using the hybrid Heyd-Scuseria-Ernzerhof (HSE06) exchange-correlation functional;[48] norm-conserving fully relativistic pseudopotentials of PseudoDojo-SO type[47,49] for describing electron-core interactions; and the PseudoDojo (medium) numerical linear combination of atomic orbitals basis set.[49] The energy mesh cutoff for the real-space grid is chosen as 51 Hartree, and the k-point grid 9 × 9 × 1 is used for the self-consistent calculations. The spectral function $A(E;\ k_x, k_y, z) = -(1/\pi)\ Im[G(E;\ k_x, k_y, z)]$ is plotted: i) in Figure S8a (Supporting Information) by varying E and k_y (while $k_x = 0$) along a high symmetry path in the Brillouin zone; or ii) in Figure 4a and Figure S8b (Supporting Information) (where the z-coordinate is 15 Å below the surface), by varying k_x and k_y at fixed energy $E = 1.9$ eV (equivalent to a photon energy of 520 nm), while plotting its spin-resolved version as a vector field of spin-momentum-locked spin textures.

Photoconductivity Phenomena from Floquet–Keldysh GF: Figure S9 (Supporting Information) depicts a 1D TB model of gapped two-terminal devices employed in Floquet–Keldysh GF photo-assisted quantum transport function calculations. The unit cell of the Rice-Mele TB chain contains two sites, i.e., it has the size of $2a$, where a is the lattice spacing. The Hamiltonian of the Rice-Mele active region is given by

$$\hat{H} = \sum_n \hat{c}_n^\dagger \left((-1)^n \frac{D}{2}\hat{\sigma}_0 - g\mu_B B\hat{\sigma}_z \right) \hat{c}_n - \sum_n \hat{c}_n t_n \hat{c}_{n+1} + h.c. \tag{4}$$

here $\hat{c}_n = (\hat{c}_{n,\uparrow}, \hat{c}_{n,\downarrow})$, is a row vector containing operators that annihilate an electron with spin ↑ ↓ at site n; $\hat{c}_n^\dagger$ is its Hermitian conjugate containing operators that create an electron in the respective state; ± $D/2$ is the

staggered on-site potential opening energy gap[37] in the density of states of the whole device (inset of Figure S9, Supporting Information); $\mathbf{B} = B\mathbf{e}_z$ is a homogeneous applied magnetic field along the *z*-axis with a unit vector $\mathbf{e}_z$; $\hat{\sigma}_0$ is the unit 2×2 matrix, and $\hat{\sigma}_\alpha$ is the Pauli matrix for $\alpha = x, y, z$ axis; g is the g-factor and μ_B is the Bohr magneton, and electrons hop between the nearest-neighbor sites with hopping parameter $t_n = (\gamma_n \hat{\sigma}_0 + i\gamma_{SO}\hat{\sigma}_\gamma)$ that is 2×2 matrix due to the Rashba SOC of strength γ_{SO} and using $\gamma_n = \gamma + \frac{\gamma_D}{2}(-1)^n$ for spin-independent hopping with staggered hopping γ_D, which is present even if SOC is switched off (solid lines in Figure 4b). For quantum transport simulations in Figure 5b–d, $\gamma_D = 0.6\gamma$, $D = 0.2\gamma$ was used in the active Rice-Mele region; $\gamma_D = \gamma_{SO} = D = 0$ in the left and right (Figure S9, Supporting Information) metallic semi-infinite electrodes modeled by 1D TB chains, and γ sets the unit of energy for all other quantities. Note that the Rice–Mele active region contains $N = 20$ sites, which ensures that the active region remains gapped, i.e., that evanescent states from two semi-infinite electrodes do not overlap the induced nonzero density of states in the inset of Figure S9 (Supporting Information).

The laser light is chosen to be linearly polarized in the *x*-direction. Its electric field **E** is introduced into the Hamiltonian using the Peierls substitution[50,51]

$$t_n \rightarrow t_n\, e^{-ie/\hbar \int_{r_n}^{r_{n+1}} dr \cdot A(r,\, t)} = t_n\, e^{izcos(\omega t)} \tag{5}$$

where the vector potential is $A(t) = e_x\, cos(\omega t)\frac{E_0}{\omega}$, so that the corresponding electric field is $E(t) = \partial A(t)/\partial t$ while the relativistic magnetic field was neglected of the laser light and its effect on electron spin. Here $z = aeE_0/(\hbar\omega)$ is a dimensionless parameter customarily used[34,37] to quantify the magnitude of the electric field of light, as employed in Figure 4. Due to the Peierls phase in Equation (5), the Hamiltonian becomes time-dependent. However, since time dependence is periodic, by switching to the time-independent Floquet Hamiltonian,[32,34] it is possible to compute quantum transport without time-evolving[38] Keldysh GF, but at the price of handling infinite matrices[36,37] of Floquet Hamiltonian and Floquet-Keldysh GF. Photocurrent current via Equation (13) in Ref. [41], which ensures charge-conservation was computed,[36] i.e., that current is identical in the left and right lead of the device in Figure S9 (Supporting Information) for any truncation of infinite matrices required in numerical calculations in Figure 4. the current convergence was checked by increasing the number of retained submatrices $2N_{ph} + 1$ within the truncated Floquet Hamiltonian,[46] assuming that current is converged if $|[I(Nph) - I(Nph - 1)]/|I(Nph)| < \delta$. For the chosen tolerance of $\delta = 0.1$ this typically requires $Nph = 8$. Finally, from the computed photocurrent in the absence and presence of applied magnetic field $B = Be_z$ in Equation (4), resistance was obtained $R_0 = I(B = 0)/V_{sd}$ plotted in Figure 4b and MR plotted in Figure 4b,c, which also requires $R_B = I(B \neq 0)/V_{sd}$.

Supporting Information

Supporting Information is available from the Wiley Online Library or from the author.

Acknowledgements

The authors thank H.Y.L. for her help with experiments. Z.L. is grateful for the financial support from the National Natural Science Foundation of China (Grants No. 52371197, 51671139), and the Natural Science Foundation of Zhejiang Province (Grant No. LY21F050001). M.F. is grateful for the financial support from the National Natural Science Foundation of China (Grant No.12074335) and the National Key R & D Program of China (Grant No. 2016YFA0300402). J.V.-M. and B.K.N. were supported by the US NSF through the University of Delaware Materials Research Science and Engineering Center, DMR-2011824.

Conflict of Interest

The authors declare no conflict of interest.

Author Contributions

Z.L. and B.W. designed the experiments. Z.L. and T.W. performed synthesis experiments and transport property measurements. Y.L. performed optical measurements. K.D. performed DFT calculations, and J.V.M. and B.K.N. performed Floquet–Keldysh calculations. Z.L., M.F., S.F., and B.W. performed data analysis. Z.L., B.W., and B.K.N. primarily wrote the paper, with all authors contributing.

Data Availability Statement

The data that support the findings of this study are available in the supplementary material of this article.

Keywords

colossal magnetoresistance, light-induced hall resistance, photoexcited hot carrier, spin-orbit coupling

Received: December 31, 2024
Revised: March 4, 2025
Published online:

[1] M. L. Brongersma, N. J. Halas, P. Nordlander, *Nat. Nanotech.* **2015**, *10*, 25.
[2] I. Ahmed, L. Shi, H. Pasanen, P. Vivo, P. Maity, M. Hatamvand, Y. Zhan, *Light Sci. Appl.* **2021**, *10*, 174.
[3] M. Massicotte, G. Soavi, A. Principi, K.-J. Tielrooij, *Nanoscale* **2021**, *13*, 8376.
[4] A. J. Nozik, *Nat. Energy* **2018**, *3*, 170.
[5] M. Ren, X. Qian, Y. Chen, T. Wang, Y. Zhao, *J. Hazard. Mater.* **2022**, *426*, 127848.
[6] M. Riede, D. Spoltore, K. Leo, *Adv. Energy Mater.* **2021**, *11*, 2002653.
[7] M. T. Sajjad, A. Ruseckas, I. D. W. Samuel, *Mater* **2020**, *3*, 341.
[8] L. H. Zeng, D. Wu, J. Jie, X. Ren, X. Hu, S. P. Lau, Y. Chai, Y. H. Tsang, *Adv. Mater.* **2020**, *32*, 2004412.
[9] S. Linic, S. Chavez, R. Elias, *Nat. Mater.* **2021**, *20*, 916.
[10] M. Vafaie, J. Z. Fan, A. M. Najarian, O. Ouellette, L. K. Sagar, K. Bertens, B. Sun, F. P. G. de Arquer, E. H. Sargent, *Matter* **2021**, *4*, 1042.
[11] H.-P. Wang, S. Li, X. Liu, Z. Shi, X. Fang, J.-H. He, *Adv. Mater.* **2021**, *33*, 2003309.
[12] L. A. Zhou, J. M. P. Martirez, J. Finzel, C. Zhang, D. F. Swearer, S. Tian, H. Robatjazi, M. Lou, L. Dong, L. Henderson, P. Christopher, E. A. Carter, P. Nordlander, N. J. Halas, *Nat. Energy* **2020**, *5*, 61.
[13] B. A. Bernevig, T. L. Hughes, S. C. Zhang, *Phys. Rev. Lett.* **2005**, *95*, 066601.
[14] P. Li, H. Dery, *Phys. Rev. Lett.* **2011**, *107*, 107203.
[15] V. Sverdlov, S. Selberherr, *Phys. Rep.* **2015**, *585*, 1.
[16] R. Niu, W. K. Zhu, *J. Phys.: Condens. Matter* **2022**, *34*, 113001.
[17] M. N. Ali, J. Xiong, S. Flynn, J. Tao, Q. D. Gibson, L. M. Schoop, T. Liang, N. Haldolaarachchige, M. Hirschberger, N. P. Ong, R. J. Cava, *Nature* **2014**, *514*, 205.
[18] C. Shekhar, A. K. Nayak, Y. Sun, M. Schmidt, M. Nicklas, I. Leermakers, U. Zeitler, Y. Skourski, J. Wosnitza, Z. Liu, Y. Chen, W. Schnelle, H. Borrmann, Y. Grin, C. Felser, B. Yan, *Nat. Phys.* **2015**, *11*, 645.

[19] B. Chen, X. Duan, H. Wang, J. Du, Y. Zhou, C. Xu, Y. Zhang, L. Zhang, M. Wei, Z. Xia, C. Cao, J. Dai, M. Fang, J. Yang, *npj Quantum Mater.* **2018**, *3*, 40.
[20] W. L. Peng, J. Y. Zhang, L. S. Luo, G. N. Feng, G. H. Yu, *J Appl. Phys.* **2019**, *125*, 093906.
[21] W. Li, Z. Yang, M. Sun, J. Dong, *Appl. Phys. Rev.* **2022**, *9*, 100077.
[22] C.-Z. Chang, J. Zhang, X. Feng, J. Shen, Z. Zhang, M. Guo, K. Li, Y. Ou, P. Wei, L.-L. Wang, Z.-Q. Ji, Y. Feng, S. Ji, X. Chen, J. Jia, X. Dai, Z. Fang, S.-C. Zhang, K. He, Y. Wang, L. Lu, X.-C. Ma, Q.-K. Xue, *Science* **2013**, *340*, 167.
[23] Z. Li, Y. Chen, R. Guo, S. Wang, W. Wang, T. Wang, S. Zhao, J. Li, J. Wu, Z. Jin, S. Wang, B. Wei, *Adv. Mater.* **2024**, *36*, 2405724.
[24] B. Huang, D. J. Monsma, I. Appelbaum, *Phys. Rev. Lett.* **2007**, *99*, 177209.
[25] I. Gierz, T. Suzuki, E. Frantzeskakis, S. Pons, S. Ostanin, A. Ernst, J. Henk, M. Grioni, K. Kern, C. R. Ast, *Phys. Rev. Let.* **2009**, *103*, 046803.
[26] R. Winkler, *Spin-Orbit Coupling Effect in Two-Dimensional Electron and Hole Systems*, Springer, Cham **2003**.
[27] S. Ito, M. Schüler, M. Meierhofer, S. Schlauderer, J. Freudenstein, J. Reimann, D. Afanasiev, K. A. Kokh, O. E. Tereshchenko, J. Güdde, M. A. Sentef, U. Höfer, R. Huber, *Nature* **2023**, *616*, 696.
[28] A. Galler, A. Rubio, O. Neufeld, *J. Phys. Chem. Lett.* **2023**, *14*, 11298.
[29] J. M. Marmolejo-Tejada, K. Dolui, P. Lazic, P.-H. Chang, S. Smidstrup, D. Stradi, K. Stokbro, B. K. Nikolic, *Nano Lett.* **2017**, *17*, 5626.
[30] K. Dolui, B. K. Nikolić, *Phys. Rev. Mater.* **2020**, *4*, 104007.
[31] M. Buscema, J. O. Island, D. J. Groenendijk, S. I. Blanter, G. A. Steele, H. S. J. van der Zant, A. Castellanos-Gomez, *Chem. Soc. Rev.* **2015**, *44*, 3691.
[32] A. Eckardt, E. Anisimovas, *New J. Phys.* **2015**, *17*, 093039.
[33] G. Stefanucci, R. van Leeuwen, *Nonequilibrium ManyBody Theory of Quantum Systems: A Modern Introduction*, Cambridge University Press, Cambridge **2025**.
[34] T. Oka, S. Kitamura, *Annu. Rev. Condens. Matter Phys.* **2019**, *10*, 387.
[35] I. Esin, M. S. Rudner, N. H. Lindner, *Sci. Adv.* **2020**, *6*, eaay4922.
[36] F. Mahfouzi, J. Fabian, N. Nagaosa, B. K. Nikolic, *Phys. Rev. B* **2012**, *85*, 054406.
[37] U. Bajpai, M. J. H. Ku, B. K. Nikolić, *Phys. Rev. Res.* **2020**, *2*, 033438.
[38] U. Bajpai, B. S. Popescu, P. Plecháč, B. K. Nikolić, L. E. F. Foa Torres, H. Ishizuka, N. Nagaosa, *J. Phys. Mater.* **2019**, *2*, 025004.
[39] J. K. Asbóth, L. Oroszlány, A. Pályi, *A Short Course on Topological Insulators: Band Structure and Edge States in One and Two Dimensions*, Springer, Cham, **2016**.
[40] S. Imai, A. Ono, S. Ishihara, *Phys. Rev. Lett.* **2020**, *124*, 157404.
[41] L. Zhou, H. Song, K. Liu, Z. Luan, P. Wang, L. Sun, S. Jiang, H. Xiang, Y. Chen, J. Du, *Sci. Adv* **2018**, *4*, eaao3318.
[42] T. Hartman, Z. Sofer, *ACS Nano* **2019**, *13*, 8566.
[43] J. Qiu, H. Fu, Y. Xu, A. I. Oreshkin, T. Shao, H. Li, S. Meng, L. Chen, K. Wu, *Phys. Rev. Lett.* **2015**, *114*, 126101.
[44] P. B. Alers, R. T. Webber, *Phys. Rev.* **1953**, *91*, 1060.
[45] Y. Tokura, *Rep. Prog. Phys.* **2006**, *69*, 797.
[46] Q. Zhou, D. Rhodes, Q. R. Zhang, S. Tang, R. Schönemann, L. Balicas, *Phys. Rev. B* **2016**, *94*, 121101.
[47] S. Smidstrup, T. Markussen, P. Vancraeyveld, J. Wellendorff, J. Schneider, T. Gunst, B. Verstichel, D. Stradi, P. A. Khomyakov, U. G. Vej-Hansen, M.-E. Lee, S. T. Chill, F. Rasmussen, G. Penazzi, F. Corsetti, A. Ojanperä, K. Jensen, M. L. N. Palsgaard, U. Martinez, A. Blom, M. Brandbyge, K. Stokbro, *J. Phys.: Condens. Matter* **2020**, *32*, 015901.
[48] J. Heyd, G. E. Scuseria, M. Ernzerhof, *J. Chem. Phys.* **2003**, *118*, 8207.
[49] M. J. van Setten, M. Giantomassi, E. Bousquet, M. J. Verstraete, D. R. Hamann, X. Gonze, G.-M. Rignanese, *Comp. Phys. Comm.* **2018**, *226*, 39.
[50] G. Panati, H. Spohn, S. Teufel, *Commun. Math. Phys.* **2003**, *242*, 547.
[51] J. Li, D. Golez, G. Mazza, A. J. Millis, A. Georges, M. Eckstein, *Phys. Rev. B* **2020**, *101*, 205140.